# Multichannel Electrophysiological Recording With Spike Detection and Sorting in a Duty-Cycled Wireless Optogenetic Headstage

Nishat T. Tasneem, *Student Member, IEEE*, Dipon K. Biswas, *Student Member, IEEE*,
Sakib Reza, *Student Member, IEEE*, April Becker, and Ifana Mahbub, *Senior Member, IEEE*

***Abstract*—Neural signal recording and optical stimulation using implantable devices have become a ubiquitous method to treat brain disorders, yet there lie some shortcomings, such as size, weight, and functionalities of the implants. This work presents a commercial off-the-shelf (COTS) component-based miniaturized wireless optogenetic headstage with simultaneous optical stimulation and electrophysiological recording for freely moving rats. The system includes a battery-based neural stimulator consisting of a low-dropout (LDO) regulator, an oscillator, and a $\mu$LED. The electrophysiological signal recording system includes an intracortical neural probe implemented on a shape memory polymer (SMP) substrate, an array of neural amplifiers with an integrated analog-to-digital converter (ADC), a transceiver IC, and a ceramic antenna. A digital sub-1-GHz transceiver integrated with a low-power microcontroller (MCU) is used to transmit the acquired neural data to a remote receiver unit, followed by offline spike detection and sorting in LabVIEW. The front-end recording amplifiers provide a gain of 45.7 dB with the input-referred noise of 2.4 $\mu V_{\text{rms}}$. The integrated multiplexer (MUX) with the ADC allows sampling of the amplified voltage at a configurable sampling rate of 160–480 kSamples/s. The total power consumption of the stimulation and the recording system is 23 mW. The dimension of the headstage device is 13.5 × 21.3 mm, weighing 4 g without the battery. The system is experimentally validated in an in vivo setting by placing the headstage on the head of a male rat and recording the neural signals from the ventral tegmental area (VTA) of the brain. This integrative neural signal recording and spike sorting approach would be useful for the development of a closed-loop neuromodulation system.**

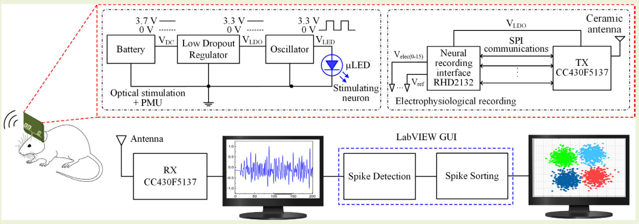

***Index Terms*— Duty-cycled optical stimulation, neuromodulation, spike sorting, wireless electrophysiological recording.**

## I. INTRODUCTION

ADVANCES in miniaturized implantable medical devices have led the way to the treatment of several neurological disorders. Modulation of activity of specific neurons via stimulation could be exploited to treat various disorders, such as Parkinson's disease, epilepsy, chronic pain, poststroke paralysis, and so on [1], [2], [3], [4], [5], [6], [7]. Compared with traditional electrical or magnetic stimulation, optogenetic stimulation is a powerful stimulation technique that can be used to precisely excite or inhibit certain types of neurons in the brain [8], [9], [10]. Using optogenetic neuromodulation, neuroscientists are able to optically stimulate the genetically engineered neurons to study and control various neural activities in the brain [11], [12], [13]. An optogenetic neuromodulation approach includes the capability of performing large-scale neural activity recording and optical stimulation using a programmable and customized modulation system. An optogenetic neuromodulation system typically includes electrophysiological recording and optical stimulation modules in order to conduct closed-loop neuromodulation to control the neural activities in relevant brain locations [14]. The recorded neural signals are wirelessly transmitted and sent to the global signal processing unit in most of the previously reported literature [13].

Manuscript received 22 July 2023; revised 5 September 2023; accepted 5 September 2023. Date of publication 13 September 2023; date of current version 31 October 2023. This work was supported by the National Science Foundation (NSF) under Grant ECCS 2309413. The associate editor coordinating the review of this article and approving it for publication was Prof. Benoit Gosselin. *(Corresponding author: Ifana Mahbub.)*

This work involved human subjects or animals in its research. Approval of all ethical and experimental procedures and protocols was granted by the University of North Texas Institutional Animal Care and Use Committee (IACUC) under Application No. 20022.

Nishat T. Tasneem and Dipon K. Biswas are with the Department of Electrical Engineering, University of North Texas, Denton, TX 76203 USA (e-mail: nishattarannumtasneem@my.unt.edu; diponkumarbiswas@my.unt.edu).

Sakib Reza and Ifana Mahbub are with the Department of Electrical and Computer Engineering, The University of Texas at Dallas, Richardson, TX 75080 USA (e-mail: sakib.reza@utdallas.edu; ifana.mahbub@utdallas.edu).

April Becker is with the Department of Behavior Analysis, University of North Texas, Denton, TX 76203 USA (e-mail: april.becker@unt.edu).

Digital Object Identifier 10.1109/JSEN.2023.3313520

These features—the simultaneous recording and stimulation of targeted neuronal populations with an iterative, closed-loop control mechanism—have many advantages for basic investigation. First, the fidelity of the intended experimental stimulation parameters and their effects would be difficult or cumbersome to directly verify the basic neuroscience experiment, particularly with chronic implantation of optical fibers, which can be technically failed at various time points. Indirect measures of stimulation efficacy, such as immediate-early gene expression [15], do not provide the electrophysiological precision necessary for characterizing stimulation effects, and neither slice physiology nor anesthetized electrophysiology provides such characterization in their intended awake, behaving context. The ability to directly verify stimulation efficacy in vivo during behavioral tests at all points in an experiment, therefore, bolsters the rigor of any such research [5], [6], [7]. In addition, the ability to modulate stimulation parameters according to electrophysiological readouts in target neurons in vivo greatly simplifies the process of identifying optical stimulation parameters in new neuronal populations or cell types. Chronically implanted optrodes setup in a closed-loop system enables not only identification and control of immediate neuronal dynamics (such as synaptic fatigue and similar processes) but also allows neuroscientists to probe for changed neuronal sensitivities over periods of days, weeks, or even months. The closed-loop setup allows neuroscientists to modulate stimulation according to the neuronal responsiveness, greatly increasing the consistency and precision of neuronal control.

Stimulation parameters include several degrees of freedom, which are specific for certain applications. The combination of parameters includes the stimulation frequency, the pulsewidth, and the output voltage delivered to the $\mu$LED [16]. Varying the stimulation parameters results in improving the efficacy of the stimulation [17]. For example, low-stimulation frequency ($<$100 Hz) improves the effectiveness of deep brain stimulation, whereas an intervention for severe gait disorder requires a high-frequency stimulation of 130–185 Hz [18]. Different stimulation frequencies are applied according to the spike trains generated from the same regions. This work utilizes the low-frequency stimulation in the ventral tegmental area (VTA), a frequent target of neural control in research investigating the effects of dopaminergic neuronal circuit function. We selected the VTA as a target not only for its popularity but also as a target of optogenetic control [19], [20], [21], [22], [23], [24], [25], but also because of its many points of clinical significance (e.g., schizophrenia [26], [27], [28], Parkinson's disease [27], [29], depression [28], [30], addiction [31], and Huntington's disease [32]), and its application to the investigation of many basic processes (e.g., basic learning and motivational processes [33], incentive salience [34], utility functions [35], prediction error [36], motor control [37], and so on).

Typically, the recording system includes neural electrodes, amplifiers, a multiplexer (MUX), an analog-to-digital converter (ADC), a transceiver module, and an antenna. Two of the significant constraints in developing a wireless headstage capable of simultaneous stimulation and multichannel recording are the limited power resource and the small form factor. This work presents a low-power analog circuitry built with standard commercial off-the-shelf (COTS) components. Arrays of 16 low-noise amplifiers are used to acquire the electrophysiological signals from the 16-channel neural probes. The neural signal recording amplifier chip RHD2132 has a built-in 16-bit ADC, which converts the amplified analog signals to digital bits [38], [39]. Here, 32 channel amplifier chips (Intan RHD2132) has been used where 16 channels have been exploited, and the other 16 have been kept left. A sub-1-GHz radio transceiver integrated with an MSP430 microcontroller (MCU) transmits the acquired neural signals to a remote receiver for further processing [40], [41]. This work utilizes only two chips, thus featuring a small form factor, while also maintaining the power budget and recording the electrophysiological signal accurately and precisely.

The utter comprehension of the neural signal recording for a target neuron depends on the detection and the sorting of the spikes from different neurons, which occur at the same neuronal surface [42], [43]. Since the spikes from different neurons can get superimposed onto each other and create correlated/uncorrelated noises, it is of great importance to conduct the spike feature extraction and sort them to the correspondent neurons. In order to extract the features from the neural signals, at first, the spikes are detected, and then, they are clustered into different groups based on their similarity of features and shapes [44]. The objective of the spike sorting is to assign each cluster to the corresponding neuron. Several techniques have been proposed for spike detection and sorting in prior works [45], [46], [47]. The spike detection algorithms can be primarily categorized into two methods: 1) manual and supervised and 2) automated and unsupervised. One of the widely used techniques for manual spike detection is the window discriminator. This method is unsuitable for large-scale recording systems, since it needs manual supervision [45], [48]. Other detection algorithms are based on the absolute-value threshold, nonlinear energy operator, and template matching [48], [49], [50]. Among these methods, nonlinear energy operator can perform well for a multielectrode setup even if the signal-to-noise ratio (SNR) is low ($<$10 dB). Considering the above constraints, this article utilizes the continuous wavelet transform (CWT)-based unsupervised spike detection algorithm implemented in LabVIEW (National Instruments, NI) [45]. This work also includes offline sorting after the spikes are detected accurately. Spikes are sorted from the detected spikes based on the features, such as the peak-to-peak amplitude of the spikes, time duration of spike trains, or interval between consecutive spikes [51]. Principal component analysis (PCA), a commonly used artificial intelligence (AI) algorithm, is one of the most widely used feature extraction methods, which reduces the dimensionality of the dataset by evaluating the variations in the neural signal. This work utilizes a PCA-based clustering technique in LabVIEW. The main objective of the implementation of this work in LabVIEW is to perform spike detection and sort in an unsupervised, faster, and accurate way. There is nothing particularly new about the detection and sorting algorithm used here; rather, the novel aspects of this work lie in the unified approach taken toward optical stimulation, neural signal recording, and spike sorting of the recorded signal.

The performance of the full system is validated in vivo with a Long–Evans rat (Charles River), which is a wild type of rat and not a genetically modified rat to validate the efficacy of optogenetic neuromodulation. Experimental results demonstrate the system's reliability in recording electrophysiological signals from 16 channels and the wireless transmission of the data. We also demonstrate the battery-powered reconfigurable optogenetic stimulation capability of the headstage system, which is only 4-g weight and is mounted on the head of the rat. Our integrated system has also a PCA and $k$-means-based spike sorting and classification GUI developed using LabVIEW, which can be used for the real-time closed-loop neuromodulation settings in the future work. The integration of the envisioned system within the NI LabVIEW framework for the purpose of spike sorting and classification signifies a novel accomplishment that is yet to be demonstrated in the current body of scientific literature. Moreover, by harnessing the capabilities of the ADC integrated within the electrophysiology interface chip (RHD 2132), the energy expenditure of the recording circuitry is significantly reduced, thus making a substantial contribution toward minimizing the system's overall footprint representing an additional element of novelty within the framework of this research undertaking. This article is organized as follows. Section II discusses the detailed design architecture of the headstage device. Section III presents the unsupervised spike detection and sorting algorithms implemented in LabVIEW. The simulation and experimental validation are provided in Section IV, followed by a concluding remark in Section V.

## II. SYSTEM OVERVIEW

The block-level diagram of the proposed optogenetic headstage is shown in the graphical abstract. The headstage is entirely built using COTS-based components. The complete system consists of two interconnected parts. The first part includes a printed circuit board (PCB), which contains the electronics for data acquisition (DAQ), wireless data transmission, and optical stimulation. The second part is a detachable implantable module, which includes the neural probe and the $\mu$LED. Two Omnetics connectors (part A79044-001 and A79045-001 pair) are used as an interface to connect the neural probe with the readout circuit PCB board. The neural recording interface allows for the conditioning and sampling of the low-amplitude extracellular action potentials (APs) as well as the local field potentials (LFPs), whose bandwidths range between 300 Hz–5 kHz and 0.1–300 Hz, respectively. The amplitude of APs is in between 50 and 500 $\mu$V, whereas the amplitude of the LFP can be up to several mV [52], [53].

### A. Implantable Neural Probe

The single-shank neural probes are utilized for reliable recording in chronic applications. In this work, a 16-electrodes probe (Model: BP-8-2x8E) from Qualia Inc., Dallas, TX, USA, is used as an interface between the neurons and the recording circuitry. The implantable shank length, width, and thickness are 8, 4, and 0.20 mm, respectively, which is the preferred length for recording the signals from the VTA. The electrode pitch is 0.5-mm thick with the dimension of 18 × 10 and 25 × 50 $\mu$m. The electrode layer is composed of sputtered iridium oxide films (SIROFs). The neural probes are fabricated using thiolene acrylate shape memory polymer (SMP) substrates that are stiff at room temperature for surgical manipulation and insertion but show a decrease in the elastic modulus by orders of magnitude at the body temperature. This limits the foreign body response by significantly reducing the mechanical mismatch between the implant and the brain tissue.

The packaged electrodes are sterilized in the following manner: the devices are loaded into a liner bag along with a gas indicator tape. The bag also contains biological indicators, such as a dosimeter and a glass ampoule containing 18 g of liquid ethylene oxide (EtO). Next, the packed liner bag is loaded into an EtO sterilizer and sealed using Velcro wrap. After 24-h sterilization cycle at room temperature and atmospheric pressure, the samples are retrieved after the 2-h purge/aeration. Following the sterilization, degassing cycles are performed to remove the residual EtO. The neural probe is placed inside a vacuum oven and kept there for 72 h at 37 °C under reduced pressure (house vacuum) for degassing cycles.

### B. Neural Signal Recording Interface

The neural recording interface IC amplifies and digitizes the measured APs and LFPs by the neural probe. The acquisition of such a high number of neural signals from multiple sites is conducted using an exclusive RHD2132 mixed-signal single-chip interface IC (Intan Technology, USA). The interface IC is packaged using a small quad flat no-lead (QFN) chip (8 × 8 mm). This customized interface provides high linearity and low input noise to appropriately measure the low amplitudes of neural waveforms. It achieves an input-referred noise of 2.4 $\mu\mathrm{V}_{\mathrm{rms}}$, with a reconfigurable bandwidth setting capability through a serial peripheral interface (SPI) bus, which allows on-the-fly reconfiguration of the bandpass filters to accommodate different input signals. Each channel includes a bandpass filter that consists of a first-order high-pass filter, the cutoff frequency of which is reconfigurable from 0.1 to 500 Hz, cascaded with a low-pass third-order Butterworth filter, and the cutoff frequency of which is reconfigurable from 0.1 to 20 kHz. The RHD2132 has a shared successive-approximation register (SAR)-ADC for all the channels through a high-speed analog MUX. All the 16 channels are sampled in a round-robin fashion to convert the analog amplified signal to the digital bits. The ADC can sample the analog output from each channel of the neural amplifier at the rate of up to 30 kSamples/s, with a resolution of 16 bits. Thus, the reconfigurable sampling rate of the ADC is in the range of 160–480 kSamples/s. In order to maintain the SPI communication to an MCU, a standard SPI interface is created through the four signals: a serial data clock (SCLK), a master in, slave out (MISO) data line, a master out, slave in data line, and an active-low chip selection pin ($\overline{\mathrm{CS}}$). In this SPI interface, the MCU works as the master and the RHD2132 as the slave. Synthetic neural signals are generated from the MATLAB and read by the LabVIEW that enables the signal to be coming from the analog output pin of the DAQ device. This analog voltage signal is then applied to the amplifier to amplify the signal. After the amplification, the on-chip ADC is used to digitize the signal. The same myDAQ device is used to process the digitized data. LabVIEW GUI is used again as the digital-to-analog converter (DAC) to reconstruct the analog neural signal. The NI measurement and automation explorer (NI MAX) from National Instrument, Austin, TX, USA, are used to apply the analog input to the amplifier and to acquire the digital output from the ADC.

### C. Wireless Transceiver

Wireless communication of the recorded data is employed using a low-power CC430F5137 chip from Texas Instruments, Dallas. This chip integrates a system-on-chip (SoC) MCU (MSP430) with an RF transceiver (CC1101) module. Since this chip also maintains the SPI interface with the RHD2132, we are able to achieve a small footprint for the headstage. The IC is packaged in a 7- × 7-mm QFN chip with a 48-pin configuration. The CC1101 operates with a supply voltage of 3.3 V. It uses two-frequency shift keying (FSK) modulation with a maximum data rate of 500 kBaud. In this work, the output transmitted power is set to 0 dBm. All the configurations of the transceiver are controlled by the MSP430 MCU. The transceiver operating in a center frequency of 868 MHz is used to transmit the neural signal data at the low-power mode to a remote base station. The receiver module is connected to the PC, where the data are reconstructed and processed using the LabVIEW GUI. The channel data are sampled in a round-robin fashion, so only the packet is sent pertaining to each channel's data at a time. Hence, the data rate of 500 kBaud is enough for the wireless system. The recorded neural signal data for all 16 channels are wirelessly transmitted in a round-robin fashion at a data rate of 500 ks/s per channel. Due to this fact, wireless transmission of data from 16 channels at 500 ks/s is sufficient.

### D. Power Management Unit

The neural recording and the stimulation system are powered by a power management unit (PMU), which includes a 3.7-V EEMB LIR2032 lithium-ion battery with a 45-mAh capacity. The lithium-ion battery can be recharged, exploiting an external adapter and reinserted in the headstage easily. As the neural recording system requires a constant 3.3-V supply, a commercially available low-dropout (LDO) voltage regulator is used to drop down the voltage to 3.3 V from the 3.7-V battery. Besides, neural stimulation requires pulse stimulation with constant voltage. Thus, an oscillator circuit is used, following the LDO circuit to provide the pulse stimulation with a constant voltage amplitude of 3.3 V.

*1) LDO Regulator:* A TPS746-Q1 ultralow-power LDO voltage regulator by Texas Instruments with a high power supply rejection ratio (PSRR) of 38 dB at 100 kHz is used to provide the constant supply voltage. The device regulates the input voltage to the nominal output voltage when the input voltage is greater than the nominal output voltage, which is 3.3 V in this work. The TPS746-Q1 has an input voltage range of 1.5–6 V and an externally adjustable output voltage range of 0.55–5.5 V. The commercial LDO is a 2- × 2-mm plastic small-outline no-lead package (WSON) packaged chip with six pins, as shown in Fig. 1(a). The input capacitor $C_{\mathrm{IN}}$ of 10 $\mu$F is used to improve the transient response, input ripple, and PSRR. If the supply voltage node of the system has a high impedance over a large frequency range, multiple capacitors can be used in parallel. An output capacitor $C_{\mathrm{out}}$ of 10 $\mu$F is used for the stability as well. The output of the LDO is adjusted using a feedback resistive divider denoted by $R_{\mathrm{FB}}$ and $R_P$. The value of the resistive dividers can be chosen based on the required output voltage using the following equation, where $V_{\mathrm{FB}}$ is the feedback voltage:

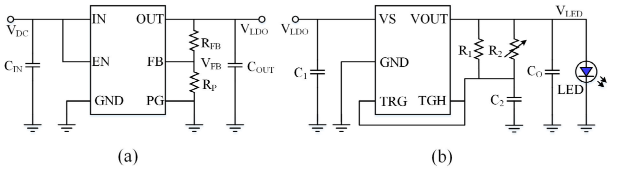

Fig. 1. (a) Schematic of the TPS746-Q1 LDO. (b) Schematic of the oscillator circuit for duty cycling the turning on/off of the stimulating LED.

$$V_{\mathrm{LDO}} = V_{\mathrm{FB}} \times \left(1 + \frac{R_{\mathrm{FB}}}{R_P}\right). \tag{1}$$

To achieve a voltage output $V_{\mathrm{LDO}}$ of 3.7 V, in this work, 10- and 4.3-k$\Omega$ resistors are used as $R_{\mathrm{FB}}$ and $R_P$, respectively, which results in a feedback voltage, $V_{\mathrm{FB}}$ of 1 V.

*2) Neural Stimulation Circuit:* The neural stimulation circuit includes a commercially available MIC1555 CMOS *RC* oscillator by Microchip to provide pulses with a precise frequency to the light source, which is a $\mu$LED in this work, as shown in Fig. 1(b). The dimension of the $\mu$LED is 0.5 × 1 × 0.4 mm$^3$. The distance between the $\mu$LED and the neural probe is kept as 1 mm, so that the signal from the neuron, which is optically stimulated by the $\mu$LED, can be recorded. The MIC1555 is a small outline transistor (SOT-23) package that can be powered from a 2.7–18-V supply voltage. An input capacitor $C_1$ of 1 $\mu$F is used to decouple the input noise. The oscillator can act as a monostable or as an astable oscillator. To use the MIC1555 as an astable oscillator, the trigger (TRG) and the threshold (THG) pin need to be connected. To set the output frequency in the astable mode, the output *RC* components need to be adjusted according to the following equation:

$$f = \frac{1}{k_1 RC} \tag{2}$$

where $R$ is the equivalent resistance of the output parallel resistance $R_1$ and $R_2$ and $C$ is the threshold capacitance $C_2$ as shown in Fig. 1(b). $k_1$ is a constant, which has a constant having a value of 1.42 for the *RC* constant range of 0.01–0.1 s. In this work, a fixed resistance of 220 $k\Omega$ is used as $R_1$, and a 1-$\mu$F capacitor is used as a threshold capacitor. To make the oscillator reconfigurable, a variable resistor $R_2$ having a range of 10–110 $k\Omega$ is used, and a load capacitor $C_o$ of 100 pF is used to make the output pulse smoother. The output pulse signal from the oscillator is then delivered to an LB-QH9G $\mu$LED by OSRAM Opto Semiconductors, which has a minimum forward voltage of 2.7 V and a minimum forward

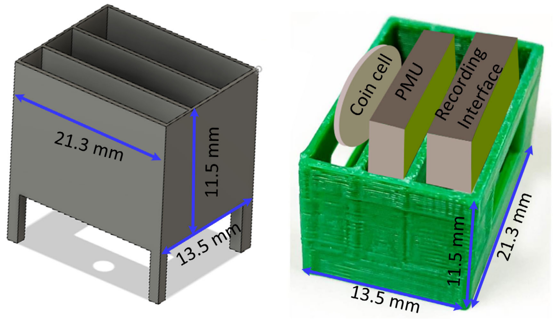

(a) (b)

Fig. 2. (a) 3-D-printed headstage architecture designed in Autodesk Fusion 360. (b) Fabricated 3-D-printed headstage using Creality Ender 3 3-D printer.

current of 5 mA. As such, given that the LDO maintains a minimum output voltage of 2.7 V, accounting for the gradual decrease in the nominal voltage of the battery, the stimulation circuit, specifically the $\mu$LED, will still continue to function.

### *E. 3-D-Printed Headstage Fabrication*

The headstage is a 3-D-printed rectangular box (21.3 × 13.5 × 11.5 mm) with three slots, which are designed to hold the lithium-ion battery (coin cell), the neural stimulation circuit and PMU, and the recording interface board, as shown in Fig. 2. It has four legs, which are cemented on the head of the rat during the in vivo experiment. Exploiting the Creality Ender 3 3-D printer, the headstage is designed using 1.75-mm polylactic acid (PLA) filament, which makes the weight of the headstage to be less than 1 g. To place the $\mu$LED and the electrode through the headstage, two holes are created at the bottom of the headstage. Fig. 2(a) shows the 3-D architecture of the headstage designed using Autodesk Fusion 360, and Fig. 2(b) shows the fabricated 3-D-printed headstage. A 38 AWG Remington wire with 10-mm length is used to connect the $\mu$LED leads with the output of the stimulation circuit. To isolate the $\mu$LED from the tissue material, the $\mu$LED and the wires are coated with polydimethylsiloxane (PDMS) coating, which is a biocompatible material.

## III. SPIKE DETECTION AND SORTING

The spike sorting process is typically a multistep procedure. The first step is the detection of the spikes, which eliminates the background noise from the spikes and aligns all the detected spikes according to the spatiotemporal points relative to the target spike waveform. The next step is the feature extraction from the detected data. After the features are extracted from the spike waveform, a reduction of the dimensionality is implemented. Here, the spikes are separated according to their features, which would best specify their identity. In the final step, spikes are grouped into different clusters according to the extracted features. The steps are described in Sections III-A and III-B as shown below.

### *A. Unsupervised Spike Detection*

In this work, CWT algorithm is adopted as an automated and unsupervised spike detection process. Since the neural amplifier has reconfigurable bandwidth, it acts as a bandpass filter (300–6000 Hz) and filters out the low-frequency and high-frequency noises. After the filtration, decomposition of the neural signal is performed with the suitable wavelet basis. Although there exist different wavelets, we have implemented one of the biorthogonal wavelets: bior1.3, which has more symmetry than other wavelets, such as db02 [45]. The block diagram of the spike detection process is shown in Fig. 3. In determining the scales, a set of scales are defined as follows [45]:

$$A = \{a_0, a_1, \ldots, a_j, \ldots, a_J\} \tag{3}$$

where $a_0$ and $a_J$ are calculated using the sampling rate of the recorded signal and the minimum and maximum width of the spikes. The sampling frequency of the recorded data used here is 20 kHz. The minimum and maximum spike widths are set as 0.5 and 1 ms, respectively, while the number of scales is chosen to be 4.

The CWT VI from the advanced signal processing toolkit in LabVIEW is used to determine the CWT coefficients from the input signal. The coefficients are defined as follows:

$$\mathrm{CWT}_s(a, \tau) = \frac{1}{\sqrt{a}} \int_{-\infty}^{\infty} s(t)\varphi_0 \times \left(\frac{t-\tau}{a}\right) dt. \tag{4}$$

Here, $s(t)$ is the input signal, and $\varphi_0(t)$ represents the mother wavelet. The other two parameters $a$ and $\tau$ are the user-defined scales and the shift of the wavelet in the $t$-direction ($dt$ being the time step size), respectively. The CWT coefficients are used to determine the hard threshold of the spike detection process from the following equation [45]:

$$T_j = \sigma_j \sqrt{2 \log_e N} \tag{5}$$

where $\sigma_j^2$ is the variance of the coefficients, $N$ is the number of samples, and $T_j$ is the automated threshold. After the spikes are detected, they are aligned relative to their threshold points. Since any misalignment among the spikes can result in the extended number of points in the feature space, eventually, the clustering of the spikes becomes more challenging. Thus, it is imperative to perform spike alignment even before the classification process. The most widely used temporal alignment method is to align the shapes of the spikes to the point of the maximal peak of the spike and store the point for a certain period. This work utilizes 1.5 ms as the spike length for alignment. The array max and min function VIs are used for determining the maximum and the minimum spike widths of the signal.

### *B. Feature Extraction and Spike Sorting*

Previous studies reported the shape of the spikes, such as amplitudes and time width of the spikes, peak-to-peak amplitude, and duration of the spike trains as the features of interest in the neural signal [54]. Although this approach is pretty straightforward, the performance of the spike sorting process deteriorates due to the noise and the inherent variance in the spike shapes. PCA is one of the most widely used algorithms for automated feature extraction in the offline analysis of the spikes. A set of orthogonal basis vectors is

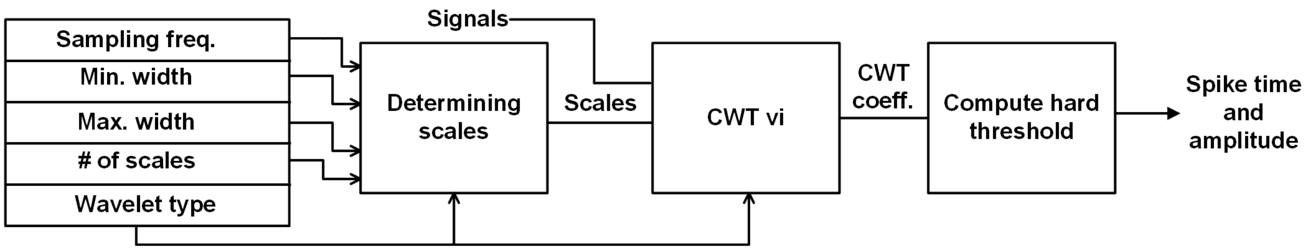

Fig. 3. Block diagram of the spike detection using CWT in LabVIEW.

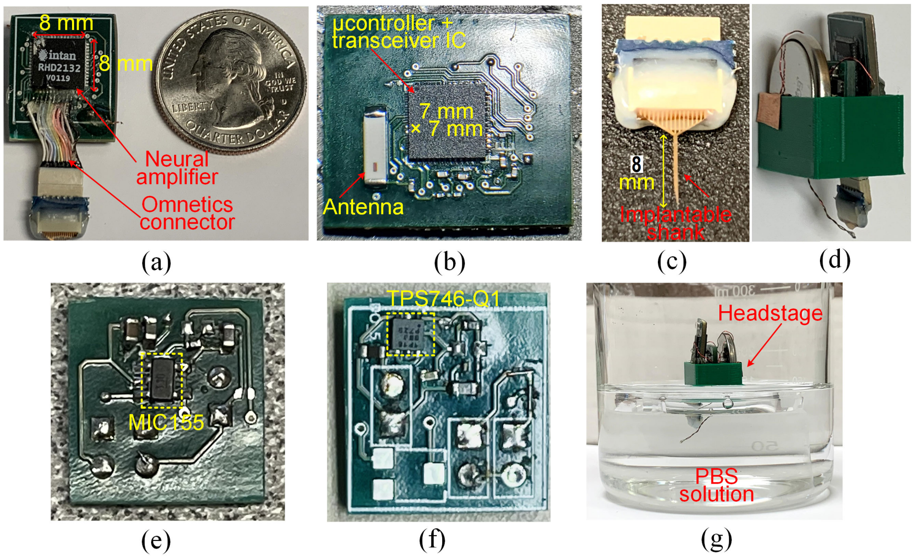

Fig. 4. (a) Top layer of the recording board. (b) Bottom layer of the board. (c) Neural probe with implantable shank. (d) Full headstage with the recording and the stimulation circuit. (e) Top layer of the stimulation board. (f) Bottom layer of the board. (g) Experimental validation of the system in PBS solution.

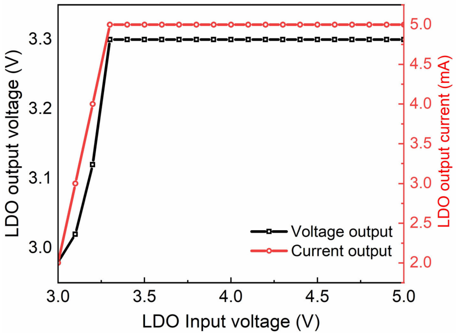

Fig. 5. Output voltage and current of the TPS746-Q1 LDO with respect to the varying input dc voltages.

estimated to interpret the variance of data, which are the original spike waveform from the acquired signal.

Any specific spike can be expressed by adding the scaled PCs as follows:

$$c_i = \sum_{n=1}^{N} \mathrm{PC}_i(n).s(n). \tag{6}$$

Here, $c_i$ is the PC coefficient, $s$ is any specific spike, $\mathrm{PC}_i$ is the $i$th PC, and $N$ is the number of samples in that particular spike. The $c_i$ is grouped together to classify the spikes.

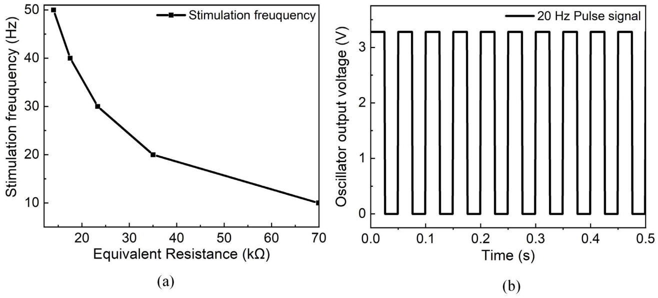

Fig. 6. (a) Stimulation frequency variation of the stimulation for varying feedback resistor. (b) Output pulse signal of 20 Hz from the MIC1555 oscillator.

## IV. IMPLEMENTATION AND MEASUREMENT RESULTS

This work is divided into two sections: optical stimulation and neural signal recording with offline spike detection and PCA-based feature extraction. The headstage includes a rigid four-layer PCB board with a thickness of 0.8 mm, which includes both the optical stimulation and neural recording system ensuring the compactness of the board, as it will be carried by the rat. The PCB has a minimum trace width of 0.2 mm and a minimum hole size of 0.15 mm. The top layer of the recording board is dedicated to the amplifier, and the bottom layer contains the transceiver and the ceramic antenna [Fig. 4(a) and (b)]. The top section holds the neural recording

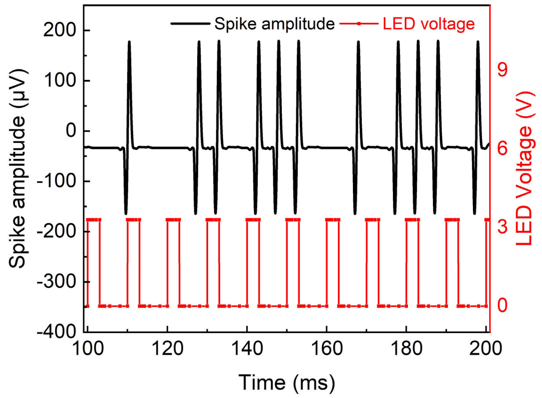

Fig. 7. LED stimulation pattern and the filtered spike waveform caused by the stimulation.

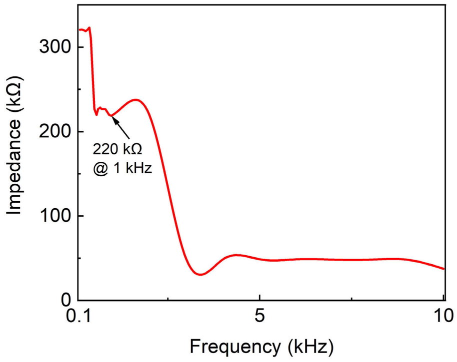

Fig. 8. Electrical characterization of neural probes inside the PBS solution.

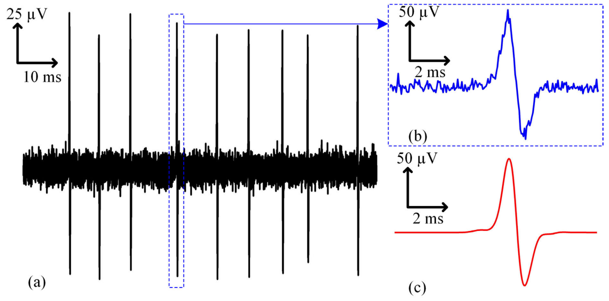

Fig. 9. (a) Reconstructed neural signal. (b) Zoomed-in view of the spike. (c) Filtered spike signal.

interface and the Omnetics connector, which connects the headstage with the implantable neural probe [Fig. 4(c)]. The whole headstage with the battery, optical stimulation, and neural recording system is shown in Fig. 4(d), where wires and layers used to connect the battery and stimulation circuit are shown to visualize the whole system. The custom probe manufactured by Qualia Labs Inc. allows recording neural activity from 16 microelectrodes, which is the number of channels of the amplifier. Fig. 4(e) and (f) presents the top and bottom layers of the optical stimulation board. The neural probe contains the implantable shank, which is immersed into the phosphate-buffered saline (PBS) solution, as shown in Fig. 4(g). The obtained results are described in detail in the following sections.

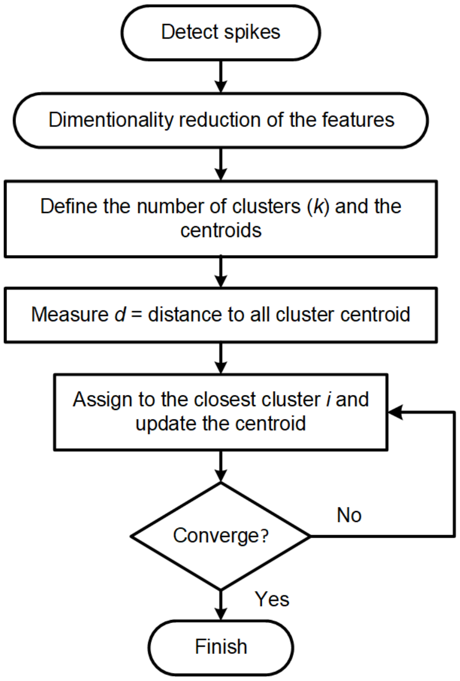

Fig. 10. Flowchart of the spike sorting process using *k*-means algorithm.

### *A. Optical Stimulation*

The PMU circuit is designed to provide 3.3 V from a 3.7-V lithium-ion battery to the analog front end and the wireless recording circuitry as well as the $\mu$LED for stimulation. The values of $R_{\mathrm{FB}}$ and $R_P$ in (1) are chosen to be 10 and 4.3 $k\Omega$ to achieve an output LDO voltage of 3.3 V and a feedback voltage of 1 V. The LDO provides a constant voltage of 3.3 V and a constant current of 10 mA when the input voltage of the LDO is above 3.3 V. Thus, the total power provided by the LDO is 33 mW. However, the forward current required for the $\mu$LED is 5 mA, so a current divider is needed at the output of the LDO to have the desired current of 5 mA as shown in Fig. 5 to operate the $\mu$LED. Fig. 6 shows the output voltage and current level for the LDO. The total power consumption of the stimulation and the recording system is 23 mW, which is powered by the PMU for almost 1.5 h.

The output voltage of the LDO is also used as the input supply voltage of the MIC1555 oscillator, which has the capability to achieve a reconfigurable pulse signal for stimulation. A fixed resistance of 220 $k\Omega$ is used as $R_1$, while a variable resistor ranging from 10 to 110 $k\Omega$ is used as $R_2$, as shown in Fig. 1. The equivalent resistance of $R_1$ and $R_2$ helps to achieve the stimulation frequency ranging from 10 to 50 Hz, as shown in Fig. 6(a). In this work, a 20-Hz oscillation frequency with a voltage amplitude of 3.3 V is used to drive the $\mu$LED. The 20-Hz pulse signal generated from the MIC1555 is shown in Fig. 6(b).

### *B. Neural Signal Recording*

The $\mu$LED stimulates the neurons at a configurable frequency of 10–50 Hz and, thus, generates the spikes. This process has been modeled utilizing the noisy spike generator used in [55]. In order to emulate the realistic surroundings, we have generated the synthetic spike waveform correlated with the LED stimulation. Some parameters, such as the spike shapes, the average amplitude of the spikes, average interspike interval, the spike firing rates, and the standard deviation of the noise, are applied to the simulator to generate the spikes. At first, the spike times are generated for the target neurons. In this work, the number of target neurons is considered as two. The spikes for a specific time interval are generated using Gaussian distribution. The spikes from the other neurons are also generated, which are correlated with one of the target neurons of interest (correlated interference). The simulator also generates the spikes from the uncorrelated neurons with the target neurons (uncorrelated interference). Since the shape of the spikes is considered as the characteristic feature of the target neuron, the shape could be modeled as the summation of the weighted delayed versions of the signals. In this work, the delay is considered to be 30 $\mu$s. Any spike lasts this amount of time in the neuron spiking surface. The number of the delay times is used as 40, which gives the duration of a spike as 1.2 ms. Finally, in order to create a realistic environment of thermal and neural interface noise, Gaussian noise is also added to the spike signals. The spike firing rate is determined from the 20%–50% duty-cycled optical stimulation frequency of 10–50 Hz, while duty-cycled optical stimulation offers flexibility to control neuromodulation.

The stimulation pattern (voltage across the $\mu$LED), which enables the stimulating current flowing through the $\mu$LED, is shown in Fig. 7 for the 20-Hz stimulation frequency. The $\mu$LED voltage stays at the constant value of 3.3 V for the 20% on period. As the stimulation by the $\mu$LED excites a group of neuronal activity rather than a single neuronal activity, there exists other neuronal interference as well for which the spike occurrence does not completely follow the $\mu$LED stimulation pattern. The synthetic neural spike signals are applied to the neural probe and transmitted wirelessly. Fig. 7 also presents the reconstructed filtered spikes having the amplitude of ~180 $\mu$V. It can be seen from the figure that the out-of-band noise and interference noises are eliminated, although the generated synthetic signal has an additional Gaussian noise correlated with the neurons. The SNR of the spike train is calculated as 32 dB. In addition, no photoelectric effect is observed in the recorded neural signal due to the stimulation of the neurons using $\mu$LEDs, as the amplifier chip has a high common mode rejection ratio (CMRR).

The neural probe is first characterized to determine the impedance. Fig. 8 shows the impedance of the probe over the frequency ranging from 0.1 to 10 kHz. The impedance is measured using AD5940BIOZ, which is a bioelectric evaluation board from Analog Devices, Norwood, MA, USA, to evaluate the bioimpedance in an electrolyte solution. A standard two-wire impedance analysis method is applied to measure the equivalent impedance of the neural probe. The Ag/AgCl electrode is used as the reference electrode, and the probe is connected as the working electrode. Typically, the spike width is ~0.5–1 ms; thus, the impedance for the neural probe is determined at 1 kHz. The impedance of the probe at 1 kHz is 220 k$\Omega$, which is the impedance of the single recording site/microelectrode. The capacitive input impedance of the neural amplifier at 1 kHz is 13 M$\Omega$.

The recorded neural signal is transmitted through the wireless transceiver at a transmitted power of 0 dBm. The distance between the transmitter and the receiver is kept as 2 m. Fig. 9(a) presents the reconstructed neural signal at the receiver end. A zoomed-in view of the reconstructed spikes is also presented in Fig. 9(b). After the additional filtering (second-order Butterworth filter in LabVIEW), the filtered spikes [Fig. 9(c)] are used in the spike detection and sorting process.

Several algorithms have been proposed for clustering the signals after they are grouped by PCA analysis. *k*-means algorithm is one of the simplest yet sophisticated approaches in spike clustering. In this work, both the PCA and the *k*-means algorithms are implemented in LabVIEW GUI, where we have used the Advanced Machine Learning Toolkit. The flowchart of the spike sorting process using the *k*-means algorithm is presented in Fig. 10. In the *k*-means clustering, at first, the number of clusters, *k*, and the cluster centroids are defined. Then, each spike is assigned to a specific cluster randomly, and then, the distances between the spike and the centroids are calculated. The spike is then assigned to the cluster with the shortest distance. Finally, the process is optimized by recomputing the position of the centroid as the mean of the spikes of that cluster. In LabVIEW GUI, the number of clusters is defined as two, since the target neurons are assumed to be two. The tolerance is set as 0.0001 for the maximum iterations of the *k*-means method as 100.

Spike detection and sorting process are performed offline by transmitting the raw signal and analyzed in LabVIEW. In order to evaluate the accuracy of the process, ground-truth data are needed. From the generated synthetic neural signal, the actual detected spikes and shapes are determined and then compared after implementing the spike sorting algorithm. The MATLAB simulator generates a 582-spike waveform emulating the real electrophysiological recordings. After the signals are received at a remote receiver, filtering and spike detection are performed. The total number of detected spikes after applying CWT is calculated as 608, resulting in an error of ~4.4%. The higher number of spikes could result from the percentage error of the computing of the hard threshold in the spike detection process.

Accuracy of the spike sorting process has been calculated using the probability of spikes reported inaccurately ($P_{\mathrm{FA}}$). A false alarm can occur to an electrode, which is affected by the surrounding noise from other electrodes, resulting in a threshold crossing of the signal. $P_{\mathrm{FA}}$ is calculated as 22% using the following equation:

$$P_{\mathrm{FA}} = \frac{\text{no. of false alarm}}{\text{no. of true negatives}}. \tag{7}$$

Probability of detection ($P_D$) is also a significant parameter for feature extraction. $P_D$ can be found from the following equation:

$$P_D = 1 - \frac{\text{no. of misses}}{\text{no. of true positives}}. \tag{8}$$

TABLE I
COMPARISON WITH THE STATE OF THE ARTS

| | [8] | [56] | [57] | [39] | This work |
|---|---|---|---|---|---|
| # of recording channels | 32 | 32 | 32 | 32 | 16 |
| ADC resolution (bits) | 16 | 16 | 16 | 16 | 16 |
| Sampling rate (kSamples/s/ch) | 20 | 20 | nr | nr | 10 – 30 |
| Amplifier bandwidth (Hz) | 0.1 – 20k | 0.1 – 20k | nr | <500 Hz (LFP) | 0.1 – 20k |
| Amplifier gain (dB) | 43.7 | nr | nr | nr | 43.7 |
| Input-referred noise ($\mu V_{rms}$) | 2.4 | 2.4 | 2.4 | 2.4 | 2.4 |
| Wireless transmission capability | Yes | Yes | No | No | Yes |
| Transceiver frequency band | 2.4 GHz | nr | nr | nr | 868 MHz |
| Transceiver data rate (kbps) | 1400 | nr | nr | nr | 500 |
| Dimension of the headstage (L × D × H) | 17 × 18 × 10 $mm^3$ | 2.8 × 1.5 × 1.1 $cm^3$ | 2.16 × 2.38 × 0.35 $mm^3$ | 3.9 × 3.9 $cm^2$ | 21.5 × 13.5 × 11.5 $mm^3$ |
| Weight of the headstage | 4.9 g | 4.4 g | 1.9 g | nr | 4 g |
| Power consumption (mW) | 175 | 122.1 | 6.9 | nr | 23 |
| Neural electrode impedance ($\Omega$) | nr | nr | nr | 10 – 500k | 200k |
| Duty cycling stimulation | No | No | No | No | Yes |
| Spike detection | Yes | No | Yes | No | Yes |
| Spike sorting | No | No | No | No | Yes |

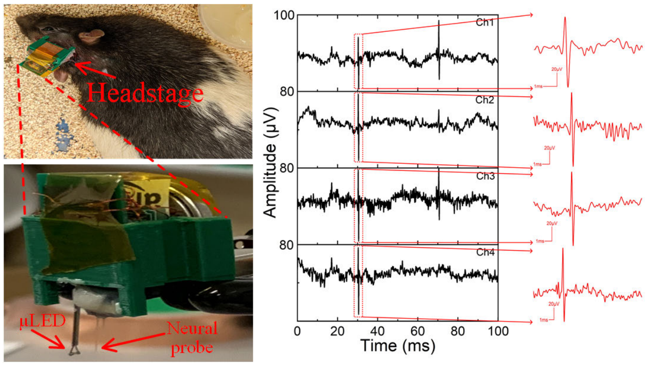

(a) (b)

Fig. 11. (a) In vivo experimental setup: freely moving rat with the headstage mounted on its head; headstage includes both the $\mu$LED and the neural probe. (b) Wirelessly recorded spontaneous neural activity.

$P_D$ is calculated in MATLAB and found to be 89%. The accuracy of the spike sorting process is validated with the high probability of $P_D$, thus making it suitable for the closed-loop neuromodulation system.

### C. In Vivo Recording

Institutional Review Boards (IRBs) approval is obtained before performing the in vivo experiment (IACUC Protocol Application Number: 20022). The SMP substrate single-shank probe is implanted inside the rat's brain. It provides mechanical stiffness for surgical treatment but softens after implantation to reduce the tissue damage. This results in an enhanced tissue response and device performance. The probe was coated with polyimide before the surgery, so no metal was exposed to the tissue surface, causing a very small amount of artifacts. The optrode was implanted stereotaxically into the VTA of the brain of a male 1.3-year-old Long–Evans rat (Charles River) weighing 963 g. The animal was first anesthetized using 3.5% isoflurane in a mixture of 1.5% $O_2$ in an anesthesia chamber. The crown of the scalp was shaved, and the animal was transferred to a stereotax, continuing to receive 2.5%–3.5% isoflurane in 1.5% oxygen for the duration of the procedure. The eyes were protected with gel to prevent drying, and a heating pad was utilized to keep the body temperature between 37° and 39°. The scalp was sterilized using chlorhexidine scrub, isopropyl alcohol (70%), and chlorhexidine solution. The scalp was injected with lidocaine, and a midline incision was created to expose the skull. A stereotaxically mounted drill was used to produce burr holes for optrode insertion and bone screws. Four bone screws surrounded the implant insertion site. The original burr hole at the target coordinates happened to produce excessive bleeding, probably because of its proximity to a medium vessel. Coordinates were, therefore, shifted by 0.1 mm to the left. After the implant was lowered to its target (relative to bregma, 0.17-mm lateral (left, adjusted), 5.8-mm posterior, and 7-mm ventral from the lower surface of dura), it was secured to the bone screws using dental cement. Buprenorphine SR (1.2 mg/kg) and 3cc supplemental saline were administered subcutaneously 15 min before the end of the procedure. After the dental cement was dried and the wireless optogenetic headstage was secured, the scalp was secured around the headstage using nylon sutures, and a further 9cc subcutaneous saline was administered in periodic 3cc increments to restore any body fluids lost during surgery. The animal's behavior and temperature were monitored until 30 min after they had regained the ability to ambulate. Fig. 11(a) shows the freely moving rat with the headstage mounted on top of its head. The first test was administered just after the animal had woken up from the procedure. Additional tests were conducted approximately 24 and 72 h later. During tests, the animal was cradled in a towel, and the battery contact from the exposed section of the headstage taped in place. The towel was removed for the measurement itself, and the animal was left to move freely. After the test, the contact was detached again and left tucked into the plastic of the implant to prevent the discharge of the battery. Each recording was conducted for a time duration of 10 min. Fig. 11(b) shows the acquired spiking activity. Here, only four channels out of 16 channels are demonstrated, as the others will give the similar recordings. The recorded neural signal from the 16 channels is transmitted wirelessly in a round-robin fashion. The recording front end

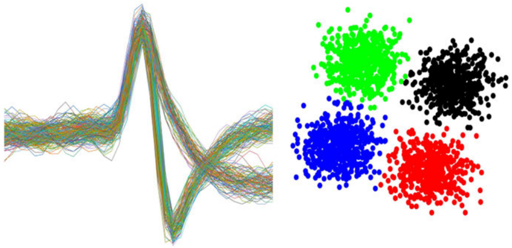
(a) (b)

Fig. 12. (a) Aligned detected spikes from the recorded data. (b) illustration of the feature space using PCA and $k$-means algorithm.

captures small spontaneous activities with the amplitudes of less than 50 $\mu$V. The LFP activity is acquired over a 3-dB bandwidth of 0.1–500 Hz through the neural probe. The lower and upper cutoff frequencies were set by the on-chip registers of RHD2132 where registers 8–13 selects the amplifier's bandwidth to record the LFPs. The original acquired signal is divided by the amplifier gain of 192 V/V. The receiver was kept within 2 ft from the headstage setup.

The spike detection and spike sorting are performed in an offline setup. The spike sorter takes the recorded data of the first day for training the algorithm and implements the feature on the recorded data of the second day. In the experiment, the threshold amplitude is set to 20 $\mu$V, and the maximum number of clusters is set to four. The algorithm is able to automatically detect the spikes, compress, and sort the spikes. The detected clusters were used to generate a trigger signal to validate the scheme. The trigger was configured to occur if four APs per cluster were found within a 100-ms time window. Fig. 12(a) shows the automatic classification results. It can be seen that the classification algorithm accurately sorted most of the APs, since each cluster encompasses a different AP waveform. The algorithm is converged to an appropriate number of clusters. The aligned spikes after the detection are shown in Fig. 12(a). The concluding step of the spike sorting process includes the clustering of the spikes from different neuron sites. Fig. 12(b) shows the clustered spikes from the aligned waveform. The clustering feature space proves that the spikes have an inter-spike interval of at least below the refractory period of 1.5 ms. The separation between the cluster centroids also clearly shows that the clusters should not be merged, which implies they are from the different target neurons. Two types of spikes are shown in Fig. 12(a), but for the whole recorded data, there were a total of four clusters, as demonstrated in Fig. 12(b), depending on the amplitude and pulsewidth variations. Table I presents a comparison among the performance parameters of the other works with those of this work. It can be seen from the table that this work includes the recording, wireless transmission, and the optical stimulation of the headstage. It also includes the duty-cycled stimulation capability, which is useful for optimizing the specific location in the brain. Another significant feature of this work is to implement unsupervised spike detection and spike sorting algorithm, which is useful for closed-loop neuromodulation. Integration of all these features has not been demonstrated in the prior works, thus making this work suitable for implementing a closed-loop optogenetic stimulation system. Nevertheless, the most challenging block of a neural recording implant is the neural amplifier. Therefore, this block needs to be elaborated in terms of designing a compact, high gain, low power, and low-noise amplifier. Also, various techniques to reduce the noise of the neural amplifier need to be assessed.

## V. CONCLUSION

This article presents the complete system of optical stimulation and electrophysiological recording system, which is able to record data using a 16-channel neural probe. The system is validated in an in vivo experimental setup in the relevant brain region to record the neural signals and send them wirelessly to the remote receiver. The system uses reconfigurable stimulation techniques that allow the system to record data for various optogenetic stimulations. The unsupervised spike sorting and spike detection help postanalyze the data to identify the brain response. This integrative and wireless recording and stimulation along with spike sorting create a path toward a truly closed-loop neuromodulation system. The benefits of this closed-loop system go beyond the sophistication of the sorted data that can be gathered. In addition, the system enables precise control of neuronal populations for neuroscientists—control that can be modulated according to either consistent or changing responsiveness in target neurons. Such a system can be used to both establish and verify the fidelity of neural control manipulations as well as to gather fine-grained, temporally extended, and behaviorally contextualized data on the characteristics of neuronal activity.

## ACKNOWLEDGMENT

The authors would like to acknowledge Qualia Labs Inc., Dallas, TX, USA, for providing the neural probes. They would also like to thank Jose E. Marcelino for helping with the fabrication of the headstages and Travis Roberts for helping with the assembly of the system.

## REFERENCES

[1] G. Gagnon-Turcotte et al., "A wireless optogenetic headstage with multichannel electrophysiological recording capability," *Sensors*, vol. 15, no. 9, pp. 22776–22797, Sep. 2015.

[2] X. Liu et al., "A fully integrated wireless compressed sensing neural signal acquisition system for chronic recording and brain machine interface," *IEEE Trans. Biomed. Circuits Syst.*, vol. 10, no. 4, pp. 874–883, Aug. 2016.

[3] S. Brenna, F. Padovan, A. Neviani, A. Bevilacqua, A. Bonfanti, and A. L. Lacaita, "A 64-channel 965-$\mu$W neural recording SoC with UWB wireless transmission in 130-nm CMOS," *IEEE Trans. Circuits Syst. II, Exp. Briefs*, vol. 63, no. 6, pp. 528–532, Jun. 2016.

[4] N. T. Tasneem and I. Mahbub, "A 2.53 NEF 8-bit 10 kS/s 0.5 $\mu$m CMOS neural recording read-out circuit with high linearity for neuromodulation implants," *Electronics*, vol. 10, no. 5, p. 590, Mar. 2021.

[5] M. Zhuo, "Cortical plasticity as a new endpoint measurement for chronic pain," *Mol. Pain*, vol. 7, no. 1, pp. 1–14, Jul. 2011.

[6] D. K. Biswas, J. H. A. Martinez, J. Daniels, A. Bendapudi, and I. Mahbub, "A novel 3-D printed headstage and homecage based WPT system for long-term behavior study of freely moving animals," in *Proc. IEEE Radio Wireless Symp. (RWS)*, Jan. 2020, pp. 268–271.

[7] T. R. Deer et al., "The appropriate use of neurostimulation: New and evolving neurostimulation therapies and applicable treatment for chronic pain and selected disease states," *Neuromodulation, Technol. Neural Interface*, vol. 17, no. 6, pp. 599–615, Aug. 2014.

[8] G. Gagnon-Turcotte, Y. LeChasseur, C. Bories, Y. Messaddeq, Y. De Koninck, and B. Gosselin, "A wireless headstage for combined optogenetics and multichannel electrophysiological recording," *IEEE Trans. Biomed. Circuits Syst.*, vol. 11, no. 1, pp. 1–14, Feb. 2017.

[9] D. K. Biswas and I. Mahbub, "A 0.09 mm$^2$ on-chip wireless power transfer system designed in 0.5 $\mu$m CMOS process for brain neuromodulation applications," *IEEE J. Electromagn., RF Microw. Med. Biol.*, vol. 4, no. 2, pp. 117–125, Jun. 2020.

[10] E. Kc et al., "Optical modulation on the nucleus accumbens core in the alleviation of neuropathic pain in chronic dorsal root ganglion compression rat model," *Neuromodulation, Technol. Neural Interface*, vol. 23, no. 2, pp. 167–176, Feb. 2020.

[11] J. Sellmeijer et al., "Hyperactivity of anterior cingulate cortex areas 24a/24b drives chronic pain-induced anxiodepressive-like consequences," *J. Neurosci.*, vol. 38, no. 12, pp. 3102–3115, Mar. 2018.

[12] K. Elina, H. C. Moon, J. Islam, H. K. Kim, and Y. S. Park, "The effect of optogenetic inhibition of the anterior cingulate cortex in neuropathic pain following sciatic nerve injury," *J. Mol. Neurosci.*, vol. 71, no. 3, pp. 638–650, Mar. 2020.

[13] R. Ameli, A. Mirbozorgi, J.-L. Néron, Y. LeChasseur, and B. Gosselin, "A wireless and batteryless neural headstage with optical stimulation and electrophysiological recording," in *Proc. 35th Annu. Int. Conf. IEEE Eng. Med. Biol. Soc. (EMBC)*, Jul. 2013, pp. 5662–5665.

[14] A. D. Mickle et al., "A wireless closed-loop system for optogenetic peripheral neuromodulation," *Nature*, vol. 565, no. 7739, pp. 361–365, Jan. 2019.

[15] K. J. Kovács, "Measurement of immediate-early gene activation-c-Fos and beyond," *J. Neuroendocrinol.*, vol. 20, no. 6, pp. 665–672, Jun. 2008.

[16] A. M. Kuncel and W. M. Grill, "Selection of stimulus parameters for deep brain stimulation," *Clin. Neurophysiol.*, vol. 115, no. 11, pp. 2431–2441, Nov. 2004.

[17] D. De Ridder, S. Perera, and S. Vanneste, "Are 10 kHz stimulation and burst stimulation fundamentally the same?" *Neuromodulation, Technol. Neural Interface*, vol. 20, no. 7, pp. 650–653, Oct. 2017.

[18] J. F. Baizabal-Carvallo and M. Alonso-Juarez, "Low-frequency deep brain stimulation for movement disorders," *Parkinsonism Rel. Disorders*, vol. 31, pp. 14–22, Oct. 2016.

[19] C. E. Bass, V. P. Grinevich, Z. B. Vance, R. P. Sullivan, K. D. Bonin, and E. A. Budygin, "Optogenetic control of striatal dopamine release in rats," *J. Neurochem.*, vol. 114, no. 5, pp. 1344–1352, Sep. 2010.

[20] W. R. Stauffer et al., "Dopamine neuron-specific optogenetic stimulation in Rhesus macaques," *Cell*, vol. 166, no. 6, pp. 1564–1571, Sep. 2016.

[21] N. E. Taylor et al., "Optogenetic activation of dopamine neurons in the ventral tegmental area induces reanimation from general anesthesia," *Proc. Nat. Acad. Sci. USA*, vol. 113, no. 45, pp. 12826–12831, Nov. 2016.

[22] K. M. Kim, M. V. Baratta, A. Yang, D. Lee, E. S. Boyden, and C. D. Fiorillo, "Optogenetic mimicry of the transient activation of dopamine neurons by natural reward is sufficient for operant reinforcement," *PLoS One*, vol. 7, no. 4, Apr. 2012, Art. no. e33612.

[23] D. Chaudhury et al., "Rapid regulation of depression-related behaviours by control of midbrain dopamine neurons," *Nature*, vol. 493, no. 7433, pp. 532–536, Jan. 2013.

[24] B. T. Saunders, J. M. Richard, E. B. Margolis, and P. H. Janak, "Dopamine neurons create Pavlovian conditioned stimuli with circuit-defined motivational properties," *Nature Neurosci.*, vol. 21, no. 8, pp. 1072–1083, Aug. 2018.

[25] K. M. Tye et al., "Dopamine neurons modulate neural encoding and expression of depression-related behaviour," *Nature*, vol. 493, no. 7433, pp. 537–541, Jan. 2013.

[26] O. D. Howes, R. McCutcheon, M. J. Owen, and R. M. Murray, "The role of genes, stress, and dopamine in the development of schizophrenia," *Biol. Psychiatry*, vol. 81, no. 1, pp. 9–20, Jan. 2017.

[27] J. Birtwistle and D. Baldwin, "Role of dopamine in schizophrenia and Parkinson's disease," *Brit. J. Nursing*, vol. 7, no. 14, pp. 832–841, Jul. 1998.

[28] A. A. Grace, "Dysregulation of the dopamine system in the pathophysiology of schizophrenia and depression," *Nature Rev. Neurosci.*, vol. 17, no. 8, pp. 524–532, Aug. 2016.

[29] N. Warren, C. O'Gorman, A. Lehn, and D. Siskind, "Dopamine dysregulation syndrome in Parkinson's disease: A systematic review of published cases," *J. Neurol., Neurosurg. Psychiatry*, vol. 88, no. 12, pp. 1060–1064, Dec. 2017.

[30] H. Hori and H. Kunugi, "Dopamine agonist-responsive depression," *Psychogeriatrics*, vol. 13, no. 3, pp. 189–195, Sep. 2013.

[31] R. A. Wise and M. A. Robble, "Dopamine and addiction," *Annu. Rev. Psychol.*, vol. 71, pp. 79–106, Jan. 2020.

[32] E. T. Koch and L. A. Raymond, "Dysfunctional striatal dopamine signaling in Huntington's disease," *J. Neurosci. Res.*, vol. 97, no. 12, pp. 1636–1654, Dec. 2019.

[33] R. A. Wise, "Dopamine, learning and motivation," *Nature Rev. Neurosci.*, vol. 5, no. 6, pp. 483–494, Jun. 2004.

[34] K. C. Berridge, "The debate over dopamine's role in reward: The case for incentive salience," *Psychopharmacology*, vol. 191, no. 3, pp. 391–431, Mar. 2007.

[35] W. R. Stauffer, A. Lak, S. Kobayashi, and W. Schultz, "Components and characteristics of the dopamine reward utility signal," *J. Comparative Neurol.*, vol. 524, no. 8, pp. 1699–1711, Jun. 2016.

[36] W. Schultz, "Dopamine reward prediction error coding," *Dialogues Clin. Neurosci.*, vol. 18, no. 1, pp. 23–32, Mar. 2016.

[37] J. Pérez-Fernández, M. Barandela, and C. Jiménez-López, "The dopaminergic control of movement-evolutionary considerations," *Int. J. Mol. Sci.*, vol. 22, no. 20, p. 11284, Oct. 2021.

[38] Y. Zheng, H. Gao, J. Zhang, Y. Wang, S. Zhang, and K. Xu, "Multi-site closed-loop stimulation strategy for seizure control with a generalized neurostimulator," in *Proc. 8th Int. IEEE/EMBS Conf. Neural Eng. (NER)*, May 2017, pp. 259–262.

[39] K. Y. Kwon, H.-M. Lee, M. Ghovanloo, A. Weber, and W. Li, "Design, fabrication, and packaging of an integrated, wirelessly-powered optrode array for optogenetics application," *Frontiers Syst. Neurosci.*, vol. 9, p. 69, May 2015.

[40] G. G. Turcotte, C.-O. D. Camaro, A. A. Kisomi, R. Ameli, and B. Gosselin, "A wireless multichannel optogenetic headstage with on-the-fly spike detection," in *Proc. IEEE Int. Symp. Circuits Syst. (ISCAS)*, May 2015, pp. 1758–1761.

[41] H.-M. Lee, K.-Y. Kwon, W. Li, and M. Ghovanloo, "A wireless implantable switched-capacitor based optogenetic stimulating system," in *Proc. 36th Annu. Int. Conf. IEEE Eng. Med. Biol. Soc.*, Aug. 2014, pp. 878–881.

[42] U. Rutishauser, E. M. Schuman, and A. N. Mamelak, "Online detection and sorting of extracellularly recorded action potentials in human medial temporal lobe recordings, in vivo," *J. Neurosci. Methods*, vol. 154, nos. 1–2, pp. 204–224, Jun. 2006.

[43] H. G. Rey, C. Pedreira, and R. Q. Quiroga, "Past, present and future of spike sorting techniques," *Brain Res. Bull.*, vol. 119, pp. 106–117, Oct. 2015.

[44] S. P. Gibson, "Neural spike sorting in hardware: From theory to practice," Ph.D. dissertation, Dept. Elect. Comput. Eng., UCLA, Los Angeles, CA, USA, 2012.

[45] Z. Nenadic and J. W. Burdick, "Spike detection using the continuous wavelet transform," *IEEE Trans. Biomed. Eng.*, vol. 52, no. 1, pp. 74–87, Jan. 2005.

[46] Z. Wang, D. Wu, F. Dong, J. Cao, T. Jiang, and J. Liu, "A novel spike detection algorithm based on multi-channel of BECT EEG signals," *IEEE Trans. Circuits Syst. II, Exp. Briefs*, vol. 67, no. 12, pp. 3592–3596, Dec. 2020.

[47] K. J. Laboy-Juárez, S. Ahn, and D. E. Feldman, "A normalized template matching method for improving spike detection in extracellular voltage recordings," *Sci. Rep.*, vol. 9, no. 1, pp. 1–12, Aug. 2019.

[48] D. Valencia and A. Alimohammad, "An efficient hardware architecture for template matching-based spike sorting," *IEEE Trans. Biomed. Circuits Syst.*, vol. 13, no. 3, pp. 481–492, Jun. 2019.

[49] X. Liu, X. Yang, and N. Zheng, "Automatic extracellular spike detection with piecewise optimal morphological filter," *Neurocomputing*, vol. 79, pp. 132–139, Mar. 2012.

[50] Y. Yang, A. Kamboh, and J. M. Andrew, "Adaptive threshold spike detection using stationary wavelet transform for neural recording implants," in *Proc. Biomed. Circuits Syst. Conf. (BioCAS)*, Nov. 2010, pp. 9–12.

[51] R. Q. Quiroga, Z. Nadasdy, and Y. Ben-Shaul, "Unsupervised spike detection and sorting with wavelets and superparamagnetic clustering," *Neural Comput.*, vol. 16, no. 8, pp. 1661–1687, Aug. 2004.

[52] L. Liu, L. Yao, X. Zou, W. Ling Goh, and M. Je, "Neural recording front-end IC using action potential detection and analog buffer with digital delay for data compression," in *Proc. 35th Annu. Int. Conf. IEEE Eng. Med. Biol. Soc. (EMBC)*, Jul. 2013, pp. 747–750.

[53] N. Tasneem and I. Mahbub, “A low-power reconfigurable readout circuit with large DC offset reduction for neural signal recording applications,” in *Proc. IEEE 63rd Int. Midwest Symp. Circuits Syst. (MWSCAS)*, Aug. 2020, pp. 521–524.

[54] M. S. Lewicki, “A review of methods for spike sorting: The detection and classification of neural action potentials,” *Netw., Comput. Neural Syst.*, vol. 9, no. 4, pp. 53–78, Jan. 1998.

[55] L. S. Smith and N. Mtetwa, “A tool for synthesizing spike trains with realistic interference,” *J. Neurosci. Methods*, vol. 159, no. 1, pp. 170–180, Jan. 2007.

[56] G. Bilodeau, G. Gagnon-Turcotte, L. L. Gagnon, C. Ethier, I. Timofeev, and B. Gosselin, “A wireless electro-optic headstage with digital signal processing and data compression for multimodal electrophysiology and optogenetic stimulation,” in *Proc. IEEE Int. Symp. Circuits Syst. (ISCAS)*, Oct. 2020, pp. 1–5.

[57] A. E. Mendrela et al., “A miniature headstage for high resolution closed-loop optogenetics,” in *Proc. IEEE Biomed. Circuits Syst. Conf. (BioCAS)*, Oct. 2017, pp. 1–4.

**Nishat T. Tasneem** (Student Member, IEEE) received the B.Sc. degree in electrical and electronic engineering from the Bangladesh University of Engineering and Technology, Dhaka, Bangladesh, in 2016. She is currently pursuing the Ph.D. degree with the Department of Electrical Engineering, University of North Texas, Denton, TX, USA.

She works as a Graduate Research Assistant with the Integrated Biomedical Circuits and Systems Laboratory (iBioCASL), University of North Texas. Her research interests include low-power circuits and systems design for biopotential recording, and self-powered biomedical sensors.

**Dipon K. Biswas** (Student Member, IEEE) received the B.S. degree from the Khulna University of Engineering and Technology, Khulna, Bangladesh, in May 2016. He is currently pursuing the Ph.D. degree with the Department of Electrical Engineering, University of North Texas, Denton, TX, USA.

He is a Graduate Research Assistant with the Department of Electrical Engineering, University of North Texas, where he is working on antenna design and optimization for wireless power transfer applications. His research interests include microwave system and antenna design, wireless power transfer, and analog and RF circuit design.

**Sakib Reza** (Student Member, IEEE) received the M.Sc. degree in electrical and electronic engineering from the Bangladesh University of Engineering and Technology, Dhaka, Bangladesh, in 2021. He is pursuing the Ph.D. degree with the Department of Electrical and Computer Engineering, The University of Texas at Dallas (UTD), Richardson, TX, USA. His M.Sc. thesis was focused on developing finger-regulated simultaneous noise and input matching (FRSNIM) technique with wideband impedance settlement for CMOS low-noise amplifiers.

He is working as a Graduate Research Assistant with the Integrated Biomedical, RF Circuits and Systems Laboratory, UTD. His research interests include the field of innovative radio frequency (RF) circuits and systems with major applications to wireless communications, medical electronics, and various emerging areas.

**April Becker** is an Assistant Professor with the Department of Behavior Analysis, University of North Texas, Denton, TX, USA, where she currently leads two laboratories. One of her laboratories investigates how particular neural systems underlie behavioral function and behavioral principles and then translationally applies behavioral and neural principles to brain injury and rehabilitation. She has another laboratory that investigates how complex arrangements of behavioral contingencies contribute to social and cultural function and evolution.

**Ifana Mahbub** (Senior Member, IEEE) received the B.Sc. degree in electrical and electronic engineering from the Bangladesh University of Engineering and Technology, Dhaka, Bangladesh, in 2012, and the Ph.D. degree in electrical engineering from The University of Tennessee, Knoxville, TN, USA, in 2017.

She is an Assistant Professor with the Department of Electrical and Computer Engineering, The University of Texas at Dallas, Richardson, TX, USA, where she is leading the Integrated Biomedical, RF Circuits and Systems Laboratory (iBioRFCASL). Her research interests include ultrawideband/mmwave phased-array antenna design for far-field wireless power transfer and vehicle-to-vehicle (V2V) communication.

Dr. Mahbub was a recipient of the National Science Foundation (NSF) Early Career Award in 2020 and the Defense Advanced Research and Project Agency (DARPA) Young Faculty Award in 2021. She is the Texas Instrument’s Early Career Chair Awardee in the Department of Electrical and Computer Engineering, The University of Texas at Dallas. She serves as the Secretary for the International Union of Radio Science (URSI) commission K and a Guest Editor for the IEEE OPEN JOURNAL OF ANTENNAS AND PROPAGATION and *Sensors* (*Multidisciplinary Digital Publishing Institute* (MDPI) *journal*).